ARTICLE

https://doi.org/10.1038/s41467-020-17517-6 OPEN

Fast growth of large-grain and continuous MoS_2 films through a self-capping vapor-liquid-solid method

Ming-Chiang Chang[1,2,9], Po-Hsun Ho[3,4,9✉], Mao-Feng Tseng[1,2,9], Fang-Yuan Lin[1,5,9], Cheng-Hung Hou[6], I-Kuan Lin[7], Hsin Wang[1,7], Pin-Pin Huang[1,5], Chun-Hao Chiang[7], Yueh-Chiang Yang[2], I-Ta Wang[7], He-Yun Du[8], Cheng-Yen Wen[3,7], Jing-Jong Shyue[6], Chun-Wei Chen[3,7], Kuei-Hsien Chen[1✉], Po-Wen Chiu[1,2✉] & Li-Chyong Chen[3,8✉]

Most chemical vapor deposition methods for transition metal dichalcogenides use an extremely small amount of precursor to render large single-crystal flakes, which usually causes low coverage of the materials on the substrate. In this study, a self-capping vapor-liquid-solid reaction is proposed to fabricate large-grain, continuous MoS_2 films. An intermediate liquid phase-$Na_2Mo_2O_7$ is formed through a eutectic reaction of MoO_3 and NaF, followed by being sulfurized into MoS_2. The as-formed MoS_2 seeds function as a capping layer that reduces the nucleation density and promotes lateral growth. By tuning the driving force of the reaction, large mono/bilayer (1.1 mm/200 μm) flakes or full-coverage films (with a record-high average grain size of 450 μm) can be grown on centimeter-scale substrates. The field-effect transistors fabricated from the full-coverage films show high mobility (33 and 49 $cm^2 V^{-1} s^{-1}$ for the mono and bilayer regions) and on/off ratio ($1 \sim 5 \times 10^8$) across a 1.5 cm × 1.5 cm region.

[1] Institute of Atomic and Molecular Sciences, Academia Sinica, Taipei 10617, Taiwan. [2] Department of Electrical Engineering, National Tsing Hua University, Hsinchu 30013, Taiwan. [3] Center of Atomic Initiative for New Materials, National Taiwan University, Taipei 106, Taiwan. [4] Department of Electrical Engineering, Stanford University, Stanford, CA 94305, USA. [5] Department of Chemistry, National Taiwan Normal University, Taipei 116, Taiwan. [6] Research Center for Applied Sciences, Academia Sinica, Taipei 11529, Taiwan. [7] Department of Materials Science and Engineering, National Taiwan University, Taipei 106, Taiwan. [8] Center for Condensed Matter Sciences, National Taiwan University, Taipei 10617, Taiwan. [9] These authors contributed equally: Ming-Chiang Chang, Po-Hsun Ho, Mao-Feng Tseng, Fang-Yuan Lin. ✉email: river770323@gmail.com; chenkh@pub.iams.sinica.edu.tw; pwchiu@ee.nthu.edu.tw; chenlc@ntu.edu.tw

Apart from graphene, transition metal dichalcogenides (TMDs) with atomic thickness are the most renowned two-dimensional (2D) materials because of their excellent electrical and optical properties[1–6]. Their robust physical properties in atmosphere enable their practical applications in novel optoelectronic devices[7,8]. For electronics, TMDs with atomic thickness, which inherently have no surface dangling bonds, are immune to mobility degradation and short channel effects in contrast to conventional three-dimensional materials, such as Si and GaAs[9–11]. Such materials have layer-dependent bandgaps from near infrared to visible regions[12,13], and thus, TMDs are favorable for energy or optical applications[7,8,14,15]. Furthermore, the difference between Berry curvature at the K and K′ valleys of monolayer TMDs generates new opportunities for valleytronics[16,17]. Despite these remarkable properties, TMDs still have limitations arising from spatial nonuniformity. Therefore, the fabrication of high-quality and large-grain films is thus crucial for TMDs. Currently, chemical vapor deposition (CVD) is the most recognized method for producing high-quality monolayer TMDs because of its low cost and scalability[18–22]. Conventional CVD methods of TMD fabrication are based on the reaction of gas-phase chalcogens (e.g., S and Se) and metal oxides (e.g., MoO_3 and WO_3)[18–22]. Generally, in gas-phase reactions, the grain size of TMDs is limited by the high nucleation density and typically is <500 μm. Recently, researchers have used various methods, which include fabricating at a high temperature[23], inserting diffusion barriers[24], and using an extremely small amount of precursors[25], to reduce nucleation density and to increase the surface diffusion length for growing large TMD crystals. These methods can produce comparatively large crystals but considerably reduce the coverage of TMD crystals[25], which hinders their practical applications.

For bulk materials, Czochralski[26,27] method enables the production of a single-crystal ingot with a diameter of up to 300 mm by vertically pulling a solid seed crystal from a liquid source[28]. This method provides the unprecedentedly high uniformity of conventional bulk materials at an ultra-large scale. Moreover, a liquid source can more easily dissolve other solid dopants than a gas–gas reaction[29]. Therefore, it is desirable to grow solid crystals from liquid sources. For the growth of TMDs, Li et al. recently proposes the vapor–liquid–solid (VLS) reaction for fabricating high-quality MoS_2 nanoribbons from a liquid precursor on a sodium chloride (NaCl) single crystal[30]. First, NaCl reacts with MoO_3 to form a eutectic compound ($Na_2Mo_2O_7$), which has a relatively lower melting point and exists in a liquid phase under growth conditions (generally 700–800 °C). Second, the sulfur vapor is rapidly dissolved into the liquid and reacts to form a solid-state monolayer MoS_2 on NaCl. However, because of the low wettability between the NaCl and liquid $Na_2Mo_2O_7$ droplets, this method can only generate MoS_2 nanoribbons, which considerably limits its application. This problem can be solved by growing on other substrates with a better wettability[31].

Herein, a self-capping vapor–liquid–solid (SCVLS) reaction, which can grow large single crystals and full-coverage TMD films, is proposed. A solid precursor comprising ultra-thin MoO_3, SiO_2, and NaF layers was used for the controllable eutectic reaction of MoO_3 and NaF at high temperature. The as-formed eutectic liquid ($Na_2Mo_2O_7$) rose to the surface and was sulfurized into MoS_2 seeds. These seeds, acted as a self-capping layer, redirected the rising liquid into a horizontal direction. The residual liquid was continuously pushed along the growth direction and eventually sulfurized to form new MoS_2 at the edge of the MoS_2 seeds. This growth mechanism enables fabrication of ultra-large (~1.1 mm) single crystals. Moreover, continuous large-area MoS_2 film with large-grain size (~450 μm) can also be fabricated using thicker precursor. By controlling the kinetic factors of this reaction, the layer number can be controlled and large bilayer MoS_2 (~200 μm) can be achieved. In this study, the quality and uniformity of MoS_2 grown using this method are evaluated through electron microscopy, optical spectroscopy, and electrical measurements. For electrical measurements, both mono- and bilayer MoS_2 field-effect transistors (FETs) show high mobility (33 and 49 $cm^2V^{-1}s^{-1}$), large on/off ratio (5×10^8), and high current density (up to 230 and 390 $\mu A\,\mu m^{-1}$). The large-grain, continuous film exhibits high performance across a 1.5 ×1.5 cm area, making the SCVLS method promising for practical applications.

Result

Material synthesis and growth mechanism. Figures 1a and S1 show that a smooth MoO_3 layer was grown on c-plane sapphire through plasma-enhanced atomic layer deposition (PEALD). SiO_2 and NaF layers were stacked on top of the MoO_3 layer through sputtering and thermal evaporation, respectively. The SiO_2 layer acted as a diffusion membrane to control the amount of MoO_3 vapor that broke the SiO_2 layer (Fig. 1b and Supplementary Fig. 2), diffused upward and reacted with the NaF layer at a temperature higher than 500 °C to form liquid-phase $Na_2Mo_2O_7$ and gas-phase MoO_2F_2 (Fig. 1b and Supplementary Fig. 3). Simultaneously, the consumption of NaF generated holes and pathways in the NaF layer, which allowed $Na_2Mo_2O_7$ and MoO_2F_2 to gradually rise to the top surface of the NaF through the pressure gradient and capillary phenomenon (Fig. 1c). Meanwhile, sulfur vapor was introduced into the system and rapidly dissolved in the eutectic liquid ($Na_2Mo_2O_7$) that rose to the surface. As discussed in the first VLS paper, the products of this VLS reaction were $MoS_{2(s)}$ and sulfur oxides ($SO_{2(g)}$ and $SO_{3(g)}$)[30]. Moreover, the molten liquid surface provided a temporarily atomic-flat and defection-free surface with a low nucleation density[23,32]. The oversaturated MoS_2 precipitated as seed layers on the liquid surface (Fig. 1e). The as-formed MoS_2 seed layers blocked the route for sulfur to dissolve into the liquid and redirected the underlying liquid to move horizontally. The unsaturated liquid then emerged to the surface at the MoS_2 edge, and this was where the SCVLS reaction primarily occurred. Therefore, MoS_2 laterally grew into large crystals (Fig. 1f, g). Millimeter-sized MoS_2 single crystals were obtained using this SCVLS method. The large triangular MoS_2 flakes are single crystals in nature, as validated by diffraction analysis at multiple spots in a large flake (Supplementary Fig. 4). The zoom-in image of a MoS_2 edge exhibits many bilayer fringes (Fig. 1h), which were a result of the precipitation of the residual liquid at the edges of the MoS_2 flakes during the rapid cooling process. These fringes validate the existence of the liquid phase during growth and the aforementioned mechanism. In contrast to the conventional CVD method, wherein the nonuniform gas flow in the furnace often gives resultant film of poorer uniformity[33], extending the SCVLS method to a wafer scale is facile because the precursor rises uniformly from the bottom surface of the growth substrate. Supplementary Fig. 5 shows a full-coverage MoS_2 film grown on a sapphire of $3 \times 3\ cm^2$ (size was only limited by the CVD tube size). This process can also be extended to grow $MoSe_2$ by replacing sulfur with selenium, result of which is shown in Supplementary Fig. 6.

Characterization of as-grown material. Compared with the conventional CVD technique, the final products of this SCVLS method were more complex (Fig. 2a), which comprised two parts: the top MoS_2 layer and the complex solid products generated by the quenched liquid within the NaF matrix. During the sulfurization process, sulfur vapor was primarily dissolved into the liquid through the exposed liquid–gas

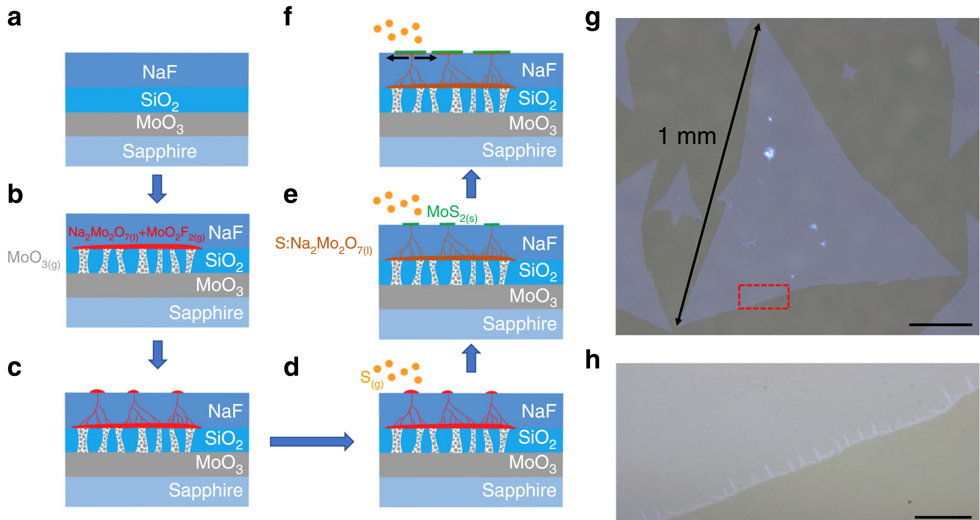

Fig. 1 Schematics of SCVLS growth mechanism and the grown MoS_2. **a** Structure of the solid precursor used for the SCVLS method. **b** At growth temperature, MoO_3 vaporized and penetrated through the SiO_2 diffusion membrane. MoO_3 and NaF reacted to form liquid-phase $Na_2Mo_2O_7$ (colored in red) at the growth temperature. **c** Through reactive digging and the capillary effect, the liquid precursor gradually rose to the NaF matrix surface. **d** Sulfur vapor was introduced into the system and started to dissolve into the $Na_2Mo_2O_7$ liquid. **e** Liquid precursor sulfurized into the MoS_2 seed layer. **f** Capped by the MoS_2, the emerging liquid was redirected horizontally and converted into MoS_2 when it contacted and dissolved sulfur vapor at the edge of the MoS_2 flakes. **g** A 1-mm MoS_2 flake grown through the SCVLS method. Scale bar is 200 µm. **h** Magnified image of the MoS_2 grain edge. The fringes at the edge indicate the presence of the liquid precursor during the growth process. Scale bar is 20 µm.

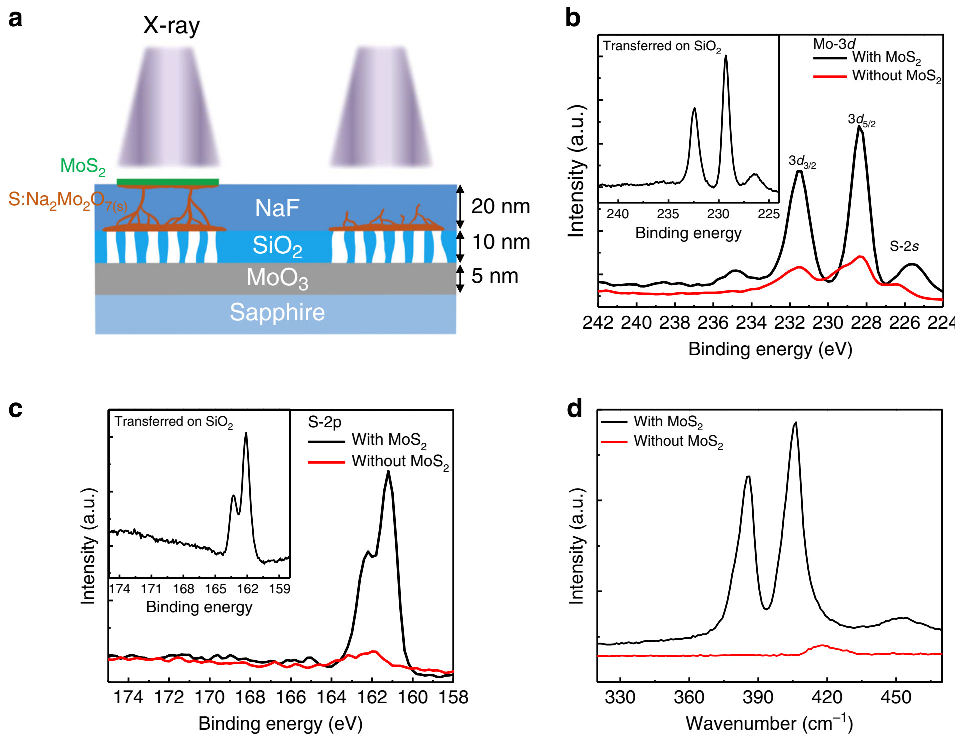

Fig. 2 Characterization of the MoS_2 monolayer and remaining solid precursors. **a** Schematic of the sampling areas of XPS. XPS data of **b** Mo-3*d* and **c** S-2*p* on sites that were covered (black) and not covered (red) with MoS_2. The broad peak of Mo-3*d* at sites that were not covered with MoS_2 indicates the complex chemical environment of Mo below the surface. Insets in **b** and **c** are the Mo-3*d* and S-2*p* of the MoS_2 film transferred onto a SiO_2 substrate. **d** Raman spectra taken form positions with (black) and without (red) MoS_2 coverage.

interface, and thus, the oversaturated liquid could continuously precipitate MoS_2 at the edge of the MoS_2 seeds. However, the reactions were not limited to the top surface. With a lower sulfur concentration, some incomplete sulfurization reactions and precipitations were observed within the NaF matrix (Supplementary Fig. 7). Upon cooling, the unsaturated liquid solidified and resided below the MoS_2 flakes or was buried in the NaF matrix (Fig. 2a). X-ray photoelectron spectroscopy (XPS)

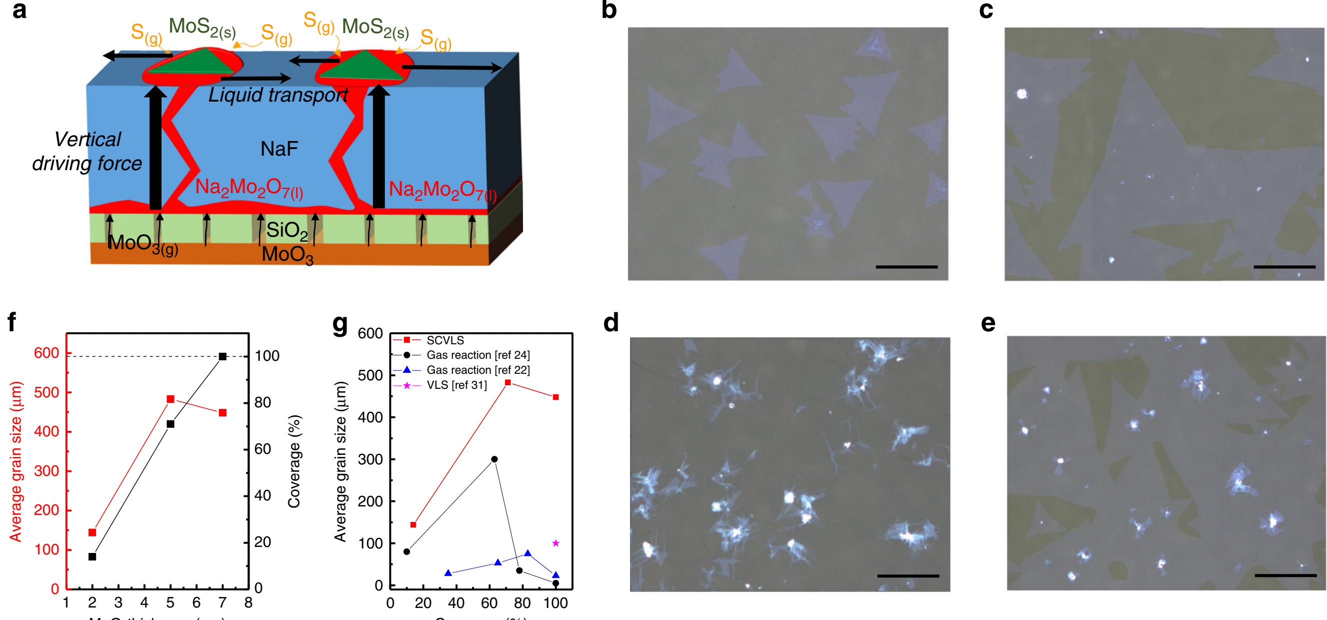

Fig. 3 Driving forces of SCVLS reaction. **a** Schematic of the vertical driving force and horizontal liquid transport. Optical microscopy images of MoS_2 grown using **b** 2-nm **c** 5-nm, and **d** 7-nm MoO_3 as a solid precursor. The growth time was 10 min. **e** 1-min growth using the same precursor sample as in **d**. The scale bars in **b**, **d**, and **e** are 200 μm and the one in **c** is 300 μm. **f** Average grain size and coverage of the MoS_2 flakes as a function of MoO_3 precursor thickness. **g** Comparison of SCVLS, VLS, and gas-phase CVD. SCVLS reaction enables a relatively large-grain size when a full-coverage film was achieved.

was used to analyze the final products. Figure 2b, c shows Mo-3*d* and S-2*p* spectra obtained from regions covered by large MoS_2 flakes and regions with the exposed NaF matrix, respectively. For a region covered with MoS_2, the Mo-3*d* peak of ~230–228 eV could be deconvoluted into sharp Mo^{4+} and broad Mo^{x+}. The Mo^{4+} signal was obtained from the top MoS_2, and the Mo^{x+} signal was obtained from the precipitates and solidified liquid phase in the NaF matrix, as shown using an XPS depth profile (Supplementary Fig. 7). With a lower sulfur concentration in the matrix, the possible products for the precipitate and quenched liquid were amorphous MoS_2, MoO_2, and MoS_xO_y, comprising the Mo^{x+} signal. In addition, a small peak at ~235 eV indicates Mo^{6+}, which is the peak from $Na_2Mo_2O_7$, indicating the presence of residual unreacted precursor below MoS_2; this supports the as-proposed horizontal transport of the liquid. For a region without MoS_2, only a small amount of sulfur diffused into the NaF matrix and reacted with the liquid below the surface. Figure 2b, c shows a considerably weaker Mo^{x+} and sulfur signal, which indicates that no liquid rose to the top surface. The resultant products were further characterized using Raman spectroscopy (Fig. 2d). The region covered with MoS_2 exhibited sharp E_{2g} and A_{1g} peaks with a spacing of 19.5 cm^{-1}, thus validating the high quality and monolayer characteristics for the as-grown MoS_2. The region that was not covered by MoS_2 exhibited no significant Raman signal, which validated the absence of any crystalline product in the NaF matrix. The as-grown monolayer MoS_2 could be readily transferred to various substrates using the conventional polymethyl-methacrylate (PMMA) method. Atomic force microscopy images and photoluminescence spectrum in Supplementary Fig. 8 and 9 also confirm the monolayer property. The insets of Fig. 2b, c show the XPS results of the as-transferred MoS_2 on silica. Compared with the as-grown sample, the transferred MoS_2 exhibited sharp and clean Mo^{4+} signals at 229.3 and 232.4 eV. The Mo–S ratio, which was calculated by integrating the area of the Mo and S signals, was 1:2, as expected for high-quality MoS_2.

Controlling the coverage and thickness of MoS_2. With a suitable sulfur source, the growth rate of SCVLS process was controlled by horizontal transport rate of the liquid. Rapid horizontal mass transport of the liquid was crucial for growing large monolayer MoS_2. The driving force stemmed from the diffusion and capillary phenomena of the high-pressure liquid and gas produced by the eutectic reaction (Fig. 3a). Because MoS_2 layers covered the top surface and confined the liquid flow, the vertical driving force was redirected horizontally, and both vertical and horizontal liquid transport was promoted with increasing amount of liquid source. The rapid SCVLS reaction could thus be performed under this condition, and the rapid growth rate abruptly increased the grain size of MoS_2. However, when the driving force was weak, the low growth rate would result in more nucleation seeds on NaF, thus reducing the average size of the MoS_2 crystals. In some regions, the weak driving force was not sufficient to push the liquid to the surface. The sulfur vapor would slowly diffuse into the NaF matrix, react with the liquid, and eventually solidify. Therefore, no MoS_2 was grown on the surface under this condition, and this phenomenon reduced the coverage of MoS_2. Here, the vertical driving force was controlled using different amounts of MoO_3 sources. Figure 3b–d shows the optical images of the as-grown MoS_2 with different thicknesses of MoO_3 precursor layers. The grain size and coverage of MoS_2 abruptly increased with the increasing thickness of MoO_3 precursor (Fig. 3f). In order to estimate the grain size of the full-coverage film (Fig. 3d), the growth time was reduced from 10 (Fig. 3d) to 1 min (Fig. 3e), to monitor the grain size before grains merged into continuous film. The average grain size of the full-coverage film was ~450 μm, which is the largest recorded average grain size for completely covered MoS_2 film. Although there are some thick islands on the film (Fig. 3d and Supplementary Fig. 10), this large-grain continuous film can still demonstrate outstanding electrical performance shown in the later section. The trend of the coverage and average grain size versus the precursor thickness in SCVLS (Fig. 3f) is very different from that for the common gas-phase reaction CVD. For gas-phase CVD, the average grain size

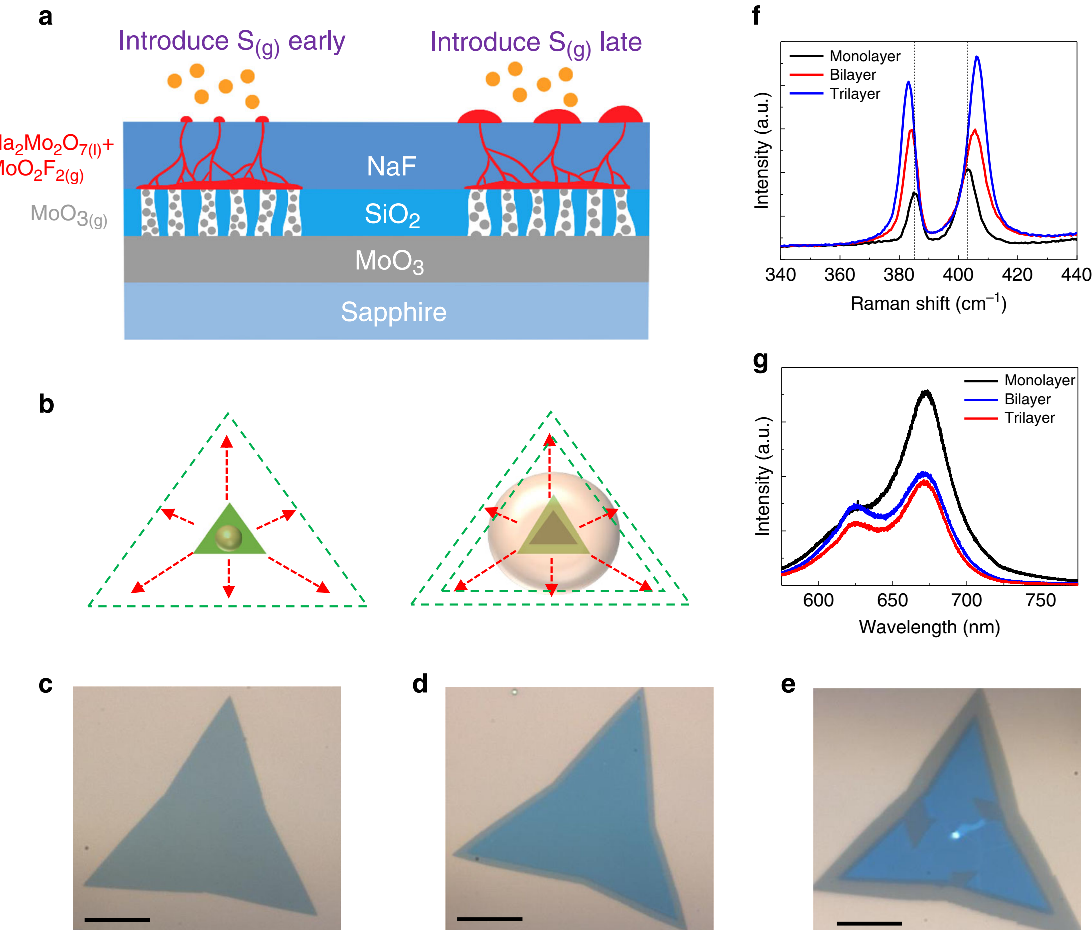

Fig. 4 Dynamic effect on SCVLS method. **a** Schematic of the timing of introducing sulfur vapor affecting the final growth product. **b** When sulfur vapor was introduced early, the $Na_2Mo_2O_7$ precursor rapidly formed the MoS_2 seed layer when exposed on the surface (left). When sulfur vapor was introduced later, the MoS_2 seed layer was formed at the solid–liquid interface, thus leaving a droplet of the liquid precursor on top of the interface. This droplet was later sulfurized into the second layer of MoS_2 (right). Optical images of the transferred **c** monolayer, **d** bilayer, and **e** trilayer MoS_2. Scale bars are 50 µm. **f** Raman and **g** photoluminescence spectra of the monolayer, bilayer, and trilayer MoS_2.

of the continuous film is reduced by a factor of 10–100 compared with the largest isolated crystals because the larger amount of the precursor for growing continuous film abruptly led to the increased nucleation density and thus reduced grain size (Fig. 3g)[25,34]. However, for SCVLS method, the average grain sizes of the continuous film (450 µm) and largest isolated crystals (500 µm) are similar because of the self-capping effect and the fast transport of liquid. Furthermore, coverage of ~82% was reached within 1 min of fabrication (Fig. 3e), which demonstrates the rapid growth rate (370 µm/min, see Supplementary Fig. 11). This may be a result from the fast transport of liquid assisted by the fluoride surface, which has been shown to enhance growth rate of 2D materials[35]. The driving force and nucleation density could be further controlled by tuning the thickness of SiO_2 membranes, growth temperature, and the thickness of NaF (Supplementary Figs. 12–14).

In addition to large-grain continuous film, layer-controlled growth of bilayer and multilayer are also attractive because of the better electrical performance of few-layer MoS_2[36–39]. SCVLS can also control the layer number of MoS_2 with its special growth mechanism we proposed. In the growth condition of previous paragraphs, sulfur vapor was introduced before or during the liquid's rise to the surface. The small liquid droplets rapidly dissolved sulfur and formed monolayer MoS_2 capping seeds, which promoted the horizontal mass transport and formed large monolayer MoS_2 grains. It is noteworthy to mention that the SCVLS reaction can be dynamically controlled by changing the timing of sulfurization (Fig. 4a). When sulfur vapor was introduced later, the emerged liquid would form into a large droplet (Supplementary Fig. 15). During sulfurization, the as-formed small MoS_2 seeds were buried in the oversaturated liquid. Under this condition, fresh MoS_2 could be formed at the edge of the original seeds, and a second layer could be grown on the MoS_2 seeds (Fig. 4b). Large bilayer MoS_2 crystals could be fabricated by delaying the sulfurization timing for 2 min. Trilayer MoS_2 was occasionally observed when sulfurization is delayed. Figure 4c–e are the optical images of the transferred mono-, bi-, and trilayer MoS_2 on SiO_2/Si substrates, respectively. The clear optical contrast shows the characteristics of the mono-, bi-, and trilayers of each MoS_2. AFM images in Supplementary Fig. 16 also confirm the thickness of these samples. Figure 4d, e shows that the second and third layers are well-aligned with the bottom MoS_2 layer, thus indicating the epitaxial growth of an excess MoS_2 layer. The diffraction patterns manifest a 2H-type stacking order of the SCVLS reaction (Supplementary Fig. 17)[30]. Raman spectra in Fig. 4f further validate the layer number and strong interaction between the mono-, bi-, and trilayer MoS_2 grown using the SCVLS method. The peak separations of E_{2g} and A_{1g} are 18.0, 21.5, and 23.2 cm^{-1}, which are similar to the values previously reported for exfoliated MoS_2[40]. The strong interaction between

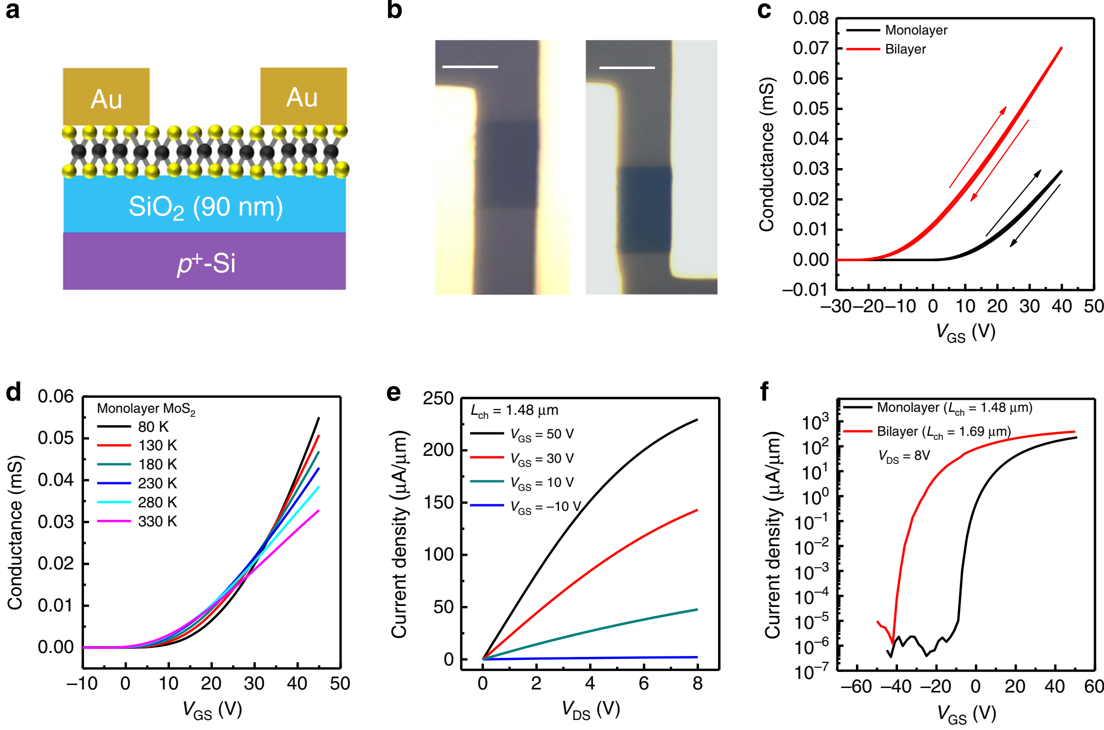

Fig. 5 Transport properties of the MoS_2 grown through the SCVLS method. **a** Schematic image of a back-gate monolayer MoS_2 transistor. **b** Optical image of a monolayer and bilayer FETs. Both scale bars are 5 µm. **c** Gate-dependent conductance of devices shown in **b**. **d** Temperature-dependent transport property of the monolayer MoS_2 FET shown in **b**. A clear MIT is observed at V_{GS} of 30 V. **e** V_{DS}-dependent source-drain current density of the monolayer device at different gate voltages. The channel length is 1.48 µm. **f** Log plot of the gate-dependent current density of the short channel mono- and bilayer devices under an 8-V source-drain bias. The on/off ratio is 5×10^8.

each layer changes the dielectric environment, thus softening the in-plane E_{2g} mode (red-shift). Moreover, the strong interaction between interlayer S increases the restoring force, thus stiffening the out-of-plane A_{1g} mode (blue shift)[40]. The photoluminescence spectra in Fig. 4g exhibit clear quenched signals for bilayer and trilayer MoS_2 because of the direct–indirect band gap transition for monolayer and bilayer MoS_2[4,6]. By employing dynamic control of sulfurization, a large bilayer single crystal (200 µm) is successfully synthesized, the grain size of which is comparable to the large bilayer crystals in the previous studies[37,38]. Moreover, the ability to change the layer number of MoS_2 by controlling the size of the droplet validated the SCVLS mechanism proposed in Fig. 1.

High-performance FET device. The electrical properties of the large monolayer MoS_2 crystal grown by the SCVLS method was examined by measuring the transport properties of MoS_2 FETs. Figure 5a shows an FET with a back-gate structure and 90-nm-thick SiO_2. Both mono- and bilayer MoS_2 FETs were fabricated as shown in Fig. 5b and Supplementary Fig. 18. Figure 5c displays the gate-dependent conductance of the MoS_2 FETs. Both devices have a very small hysteresis, indicating low defect and impurity induced trap density in the SCVLS growth and the device fabrication processes. The field-effect mobility was calculated using $\mu_{FE} = \frac{L_{CH}}{W}\frac{1}{C_G}\frac{dG}{dV_{GS}}$, where C_G, L_{CH}, W, V_{GS}, and G stand for the back-gate capacitance, channel length, channel width, back-gate voltage, and sheet conductance of the channel, respectively. Because of its higher carrier density and stronger charge screening effect, bilayer MoS_2 has a smaller threshold voltage (V_{th}) and higher mobility. The mobilities of the mono- and bilayer MoS_2 FETs are 33 and 49 $cm^2 V^{-1} S^{-1}$, respectively. These values are comparable to the exfoliated MoS_2[41] and the best reported values of CVD MoS_2 on SiO_2[38,42,43], showing the high quality of MoS_2 grown through the SCVLS method. The temperature-dependent transport also confirms the quality of SCVLS MoS_2 as shown in Fig. 5d. For the monolayer device, a clear metal–insulator transition (MIT) was observed, which is generally detected when using a high-k dielectric layer to reduce Columbic scattering in the MoS_2 channel[2]. For back-gate devices without a high-k dielectric layer, a clear MIT occurs only when using high-quality MoS_2 with a low concentration of sulfur vacancies. In general, according to the Ioffe-Regel criterion[44], MIT occurs when the critical channel conductance is approximately one quantum conductivity (e^2/h)[2,44]. If the crossover point is in a lower carrier concentration region, this directly reflects the high-mobility property of MoS_2[45,46]. The carrier concentration of the transition point is calculated using

$$n_{\mathrm{MIT}} = \frac{C_G}{e}(V_T - V_{\mathrm{MIT}}), \tag{1}$$

where V_T and V_{MIT} are the threshold voltage and voltage at which the MIT occurs, respectively[47,48]. The n_{MIT} of the SCVLS MoS_2 in this study is $4.3 \times 10^{12}\ cm^{-2}$, which is even lower than the previously reported intrinsic exfoliated MoS_2 with low S-vacancy concentration[47]. This indicated the high quality and low sulfur vacancy concentration of the MoS_2 fabricated using the SCVLS method. Figure 5e is the output characteristics of a short channel (1.48 µm, see Supplementary Fig. 19) monolayer FET at various back-gate voltages. The linear behavior in the low source-drain voltage (V_{DS}) region shows a good Ohmic property of contacts. Figure 5f presents the semi-logarithmic of the gate-controlled current density. The device on/off ratio can reach 5×10^8, with a subthreshold swing of 980 mV dec^{-1}. The maximum current

Table 1 Comparison of the different CVD methods.

Growth method	Maximum grain size (single crystal)	Mobility ($cm^2 V^{-1} s^{-1}$)	Maximum current density ($\mu A\ \mu m^{-1}$)	On/off ratio	Reference
CVD MoS_2 (MoO_3 + S, substrate control)[49]	200 µm	25		10^7	ACS Nano 2015, 9, 4611
CVD MoS_2 (MoO_3 + S, flow control)[50]	300 µm	30		10^6	Adv. Sci. 2016, 3, 1500033
CVD MoS_2 ($MoCl_5$ + DMS, NaCl catalyst)[51]	50 µm	10.4		10^7	Nanotechnology 2017, 28, 465103
CVD MoS_2 (MoO_3 + S, molten Na:glass)[32]	563 µm	24	123	10^9	Appl. Phys. Lett. 2018, 113, 202103
CVD MoS_2 (MoO_3 + S with PTAS salt)[42]	200 µm	35	270	10^7	Nano Lett. 2018, 18, 4516
CVD MoS_2 (Mo foil + S, soda-lime glass)[52]	400 µm	11.4		10^6	Nat. Commun. 2018, 9, 979
SCVLS MoS_2	1.1 mm	33	230	5×10^8	This work

All transport data were obtained from the back-gate, monolayer MoS_2 FETs for comparison.

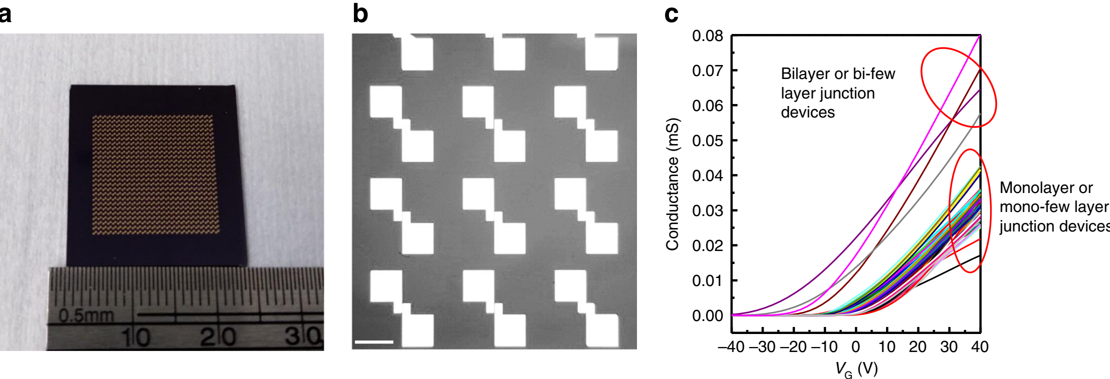

Fig. 6 Transport properties of the large-grain, continuous film. **a** Photo-image of the as-fabricated FETs across a 1.5 × 1.5-cm region. **b** Optical image of FET devices. The scale bar is 150 µm. The fine feature is shown in Supplementary Fig. 18. **c** Gate-dependent conductance of the devices across the large area.

density in the monolayer MoS_2 is 230 µA μm^{-1} (390 µA μm^{-1} for bilayer), potentially comparable to the optimal reported in consideration of the difference in contact geometry[38,42]. Table 1 lists the recently reported monolayer MoS_2 back-gate FETs. MoS_2 grown by the SCVLS method exhibits the largest grain size and remarkable electrical performance compared with other CVD techniques. The good uniformity of the large monolayer crystal is confirmed by measuring 18 FETs in a 1-mm crystal (Supplementary Fig. 20). In addition, with the capability of growing large-grain and continuous film, we fabricated hundreds of devices across a 1.5 × 1.5-cm area, as shown in Fig. 6a, b. Figure 6c is the gate-dependent conductance of a hundred devices in the whole area. Ninety percent of devices have pure monolayer channel and show high mobilities (34 ± 7 $cm^2 V^{-1} s^{-1}$) with small variation of V_{th} (4.9 ± 2.3 V). Devices have larger variation in mobility and V_{th} if their channels are bilayer, few-layer, mono-few-layer junction, or monolayer with a small few-layer flake on top. However, the mobilities are still high for all of the devices because of the large-grain monolayer underneath (Supplementary Fig. 21). This demonstrates the advantage of using the SCVLS method for practical applications.

Discussion

In summary, a new concept of growing high-quality single-crystal 2D materials from the liquid precursor was proposed using the SCVLS method. The rapid horizontal mass transport promotes the lateral growth of 2D materials and allows the growth of MoS_2 flakes as large as 1.1 mm. The self-capping effect drastically reduces the nucleation density even under large amount of precursor and results in a wafer scale, 100% coverage MoS_2 films with an average grain size of up to 450 µm. It overcomes the bottleneck of the conventional gas-phase CVD reaction, which is the trade-off between coverage and grain size. The quality and uniformity of the as-grown MoS_2 were carefully evaluated through the electrical properties of MoS_2 FETs across a large area. High-mobility MoS_2 devices are demonstrated across a 1.5 × 1.5-cm area. Moreover, this method is capable of fabricating large bilayer MoS_2 crystals by controlling the timing of sulfurization. More sophisticated sulfurization precursor such as H_2S is expected to improve the layer number control or the uniformity of continuous films. Fabricating crystals by using the liquid–solid reaction, such as in doping and alloying, is one expected niche of this SCVLS method, which provides a new approach for synthesizing industrial-grade 2D materials for practical applications in 2D electronics.

Methods

Preparation of solid precursor. 3 × 3-cm c-plane (0001) sapphire substrate was cleaned first by deionized water then sonicated in acetone and isopropyl alcohol for 20 and 5 min, respectively. MoO_3 film with well-controlled thickness was grown on top of sapphire substrates with a homemade PEALD system using $Mo(CO)_6$ as precursor and oxygen plasma as the oxidation reactant. For each deposition cycle, a $Mo(CO)_6$ precursor pulse is provided into the chamber, then the excess precursor is purged away by argon, and finally oxygen plasma (up to 200 W) is used to oxidize the precursor and form uniform MoO_3 film. Thermal evaporation can be used to replace the PEALD process for depositing MoO_3 but will result in worse MoS_2 morphology (Supplementary Fig. 22). SiO_2 film was deposited on top of MoO_3 layer by sputtering a 3-inch SiO_2 target with Ar plasma at a power density of 0.6 W/cm^2 in a radio-frequency magnetron sputtering system. NaF thin film was deposited onto the sample by heating NaF powder (Acros, 97%) loaded in a Mo boat in a high vacuum evaporator chamber (<5 × 10^{-5} torr). For sputtering and thermal evaporation film, film thickness was monitored by a quartz crystal microbalance and the deposition rate was maintained at 0.1 Ås^{-1}. Samples were attached to a spinning sample holder to obtain high uniformity.

Growth of MoS_2. High temperature growth was carried out in a 2-inch quartz tube and the temperature profile of the growth was controlled by a three-zone furnace. Sulfur powder (Aldrich, 99.98%), which was placed in an alumina crucible, and precursor sample held by a 3 × 3-cm^2 quartz plate were placed at the center of first and third hearing zone, respectively, as depicted in Supplementary Fig. 1c.

A 5 sccm H_2 and 50 sccm Ar mixed gas flow was used as carrier gas and the pressure within the quartz tube was controlled to be 30 torr. The temperature at the sample ramped up at a rate of 40 °C min^{-1} to 800 °C and was held for 10 min. Sulfur vapor was introduced by ramping up the temperature at the first zone at a rate of 15 °C min^{-1} and was held at the desired temperature during growth. After growth, the furnace was turned off and was fast-cooled using an industrial fan. The temperature ramping profile is shown in Supplementary Fig. 1d. For monolayer MoS_2 growth, A and B setpoints are reached at the same time. For bilayer MoS_2 growth, the B setpoint is reached 2 min later than the A setpoint.

Device fabrication and characterization. *p*-type heavily doped silicon wafers with 90-nm thermal oxide layers were used for back-gate FET devices. MoS_2 films/isolated crystals were transferred to wafers through a conventional PMMA method. Optical lithography and oxygen plasma were used to define the MoS_2 strips. Then, the second lithography process defined the source-drain patterns. A 50-nm gold layer was thermally evaporated under high vacuum as the source-drain and back-gate electrodes. Before measuring electrical properties, FETs were annealed at 120 °C under a 10^{-3} torr vacuum for 10 h in a probe station (Lakeshore). Gate and source-drain voltage were applied by Kethley 6487 picometers. Raman and photoluminescence spectra were measured by a confocal system equipped with a 476-nm laser. XPS spectra were obtained using PHI VersaProbe system. Transmission electron analysis (Supplementary Figs. 4, 17, and 23) was performed in JEOL AEM 2010F and JEOL AEM 2100F, which was equipped with a probe-type corrector for the spherical aberration of the objective lens. Both systems were operated at 200 kV for the analysis.

Data availability

The data that support the findings of this study are available from the corresponding author on reasonable request.

Received: 12 August 2019; Accepted: 1 July 2020;
Published online: 23 July 2020

References

1. Radisavljevic, B., Radenovic, A., Brivio, J., Giacometti, V. & Kis, A. Single-layer MoS_2 transistors. *Nat. Nanotechnol.* **6**, 147–150 (2011).
2. Radisavljevic, B. & Kis, A. Mobility engineering and a metal–insulator transition in monolayer MoS_2. *Nat. Mater.* **12**, 815–820 (2013).
3. Fang, H. et al. High-performance single layered WSe_2 p-FETs with chemically doped contacts. *Nano Lett.* **12**, 3788–3792 (2012).
4. Mak, K. F., Lee, C., Hone, J., Shan, J. & Heinz, T. F. Atomically thin MoS_2: a new direct-gap semiconductor. *Phys. Rev. Lett.* **105**, 136805 (2010).
5. Gutiérrez, H. R. et al. Extraordinary room-temperature photoluminescence in triangular WS_2 monolayers. *Nano Lett.* **13**, 3447–3454 (2012).
6. Splendiani, A. et al. Emerging photoluminescence in monolayer MoS_2. *Nano Lett.* **10**, 1271–1275 (2010).
7. Mak, K. F. & Shan, J. Photonics and optoelectronics of 2D semiconductor transition metal dichalcogenides. *Nat. Photonics* **10**, 216–226 (2016).
8. Xia, F., Wang, H., Xiao, D., Dubey, M. & Ramasubramaniam, A. Two-dimensional material nanophotonics. *Nat. Photonics* **8**, 899–907 (2014).
9. Cao, W., Kang, J., Sarkar, D., Liu, W. & Banerjee, K. 2D semiconductor FETs—projections and design for sub-10 nm VLSI. *IEEE Trans. Electron Devices* **62**, 3459–3469 (2015).
10. Xu, K. et al. Sub-10 nm nanopattern architecture for 2D material field-effect transistors. *Nano Lett.* **17**, 1065–1070 (2017).
11. Liu, H., Neal, A. T. & Ye, P. D. Channel length scaling of MoS_2 MOSFETs. *ACS Nano* **6**, 8563–8569 (2012).
12. Tongay, S. et al. Thermally driven crossover from indirect toward direct bandgap in 2D semiconductors: $MoSe_2$ versus MoS_2. *Nano Lett.* **12**, 5576–5580 (2012).
13. Sahin, H. et al. Anomalous Raman spectra and thickness-dependent electronic properties of WSe_2. *Phys. Rev. B* **87**, 165409 (2013).
14. Li, H., Shi, Y., Chiu, M.-H. & Li, L.-J. Emerging energy applications of two-dimensional layered transition metal dichalcogenides. *Nano Energy* **18**, 293–305 (2015).
15. Choi, W. et al. Recent development of two-dimensional transition metal dichalcogenides and their applications. *Mater. Today* **20**, 116–130 (2017).
16. Zhang, Y. J., Oka, T., Suzuki, R., Ye, J. T. & Iwasa, Y. Electrically switchable chiral light-emitting transistor. *Science* **344**, 725–728 (2014).
17. Mak, K. F., Xiao, D. & Shan, J. Light–valley interactions in 2D semiconductors. *Nat. Photonics* **12**, 451 (2018).
18. Lee, Y. et al. Synthesis of large-area MoS_2 atomic layers with chemical vapor deposition. *Adv. Mater.* **24**, 2320–2325 (2012).
19. Wang, X. et al. Chemical vapor deposition growth of crystalline monolayer $MoSe_2$. *ACS Nano* **8**, 5125–5131 (2014).
20. Cong, C. et al. Synthesis and optical properties of large-area single-crystalline 2D semiconductor WS_2 monolayer from chemical vapor deposition. *Adv. Opt. Mater.* **2**, 131–136 (2014).
21. Huang, J.-K. et al. Large-area synthesis of highly crystalline WSe_2 monolayers and device applications. *ACS Nano* **8**, 923–930 (2013).
22. Lin, Z. et al. Controllable growth of large–size crystalline MoS_2 and resist-free transfer assisted with a Cu thin film. *Sci. Rep.* **5**, 18596 (2015).
23. Chen, J. et al. Chemical vapor deposition of large-size monolayer $MoSe_2$ crystals on molten glass. *J. Am. Chem. Soc.* **139**, 1073–1076 (2017).
24. Lim, Y.-F. et al. Modification of vapor phase concentrations in MoS_2 growth using a NiO foam barrier. *ACS Nano* **12**, 1339–1349 (2018).
25. Lee, J. et al. Thermodynamically stable synthesis of large-scale and highly crystalline transition metal dichalcogenide monolayers and their unipolar n–n heterojunction devices. *Adv. Mater.* **29**, 1702206 (2017).
26. Czochralski, J. Ein neues verfahren zur messung der kristallisationsgeschwindigkeit der metalle. *Z. für. Phys. Chem.* **92**, 219–221 (1918).
27. Zulehner, W. Czochralski growth of silicon. *J. Cryst. Growth* **65**, 189–213 (1983).
28. Zulehner, W. Historical overview of silicon crystal pulling development. *Mater. Sci. Eng. B* **73**, 7–15 (2000).
29. Zhou, J. et al. A library of atomically thin metal chalcogenides. *Nature* **556**, 355–359 (2018).
30. Li, S. et al. Vapour–liquid–solid growth of monolayer MoS_2 nanoribbons. *Nat. Mater.* **17**, 535–542 (2018).
31. Li, S. et al. Wafer-scale and deterministic patterned growth of monolayer MoS_2 via vapor–liquid–solid method. *Nanoscale* **11**, 16122–16129 (2019).
32. Zhang, Z. et al. High-performance transistors based on monolayer CVD MoS_2 grown on molten glass. *Appl. Phys. Lett.* **113**, 202103 (2018).
33. Wang, S. et al. Shape evolution of monolayer MoS_2 crystals grown by chemical vapor deposition. *Chem. Mater.* **26**, 6371–6379 (2014).
34. Yu, H. et al. Wafer-Scale Growth and Transfer of Highly-Oriented Monolayer MoS_2 Continuous Films. *ACS Nano* **11**, 12001–12007 (2017).
35. Liu, C. et al. Kinetic modulation of graphene growth by fluorine through spatially confined decomposition of metal fluorides. *Nat. Chem.* **11**, 730–736 (2019).
36. Zheng, J. et al. High-mobility multilayered MoS_2 flakes with low contact resistance grown by chemical vapor deposition. *Adv. Mater.* **29**, 1604540 (2017).
37. Zhang, X. et al. Transition metal dichalcogenides bilayer single crystals by reverse-flow chemical vapor epitaxy. *Nat. Commun.* **10**, 598 (2019).
38. Gao, Q. et al. Scalable high performance radio frequency electronics based on large domain bilayer MoS_2. *Nat. Commun.* **9**, 4778 (2018).
39. He, T. et al. Synthesis of large-area uniform MoS_2 films by substrate-moving atmospheric pressure chemical vapor deposition: from monolayer to multilayer. *2D Mater.* **6**, 25030 (2019).
40. Li, H. et al. From bulk to monolayer MoS_2: evolution of Raman scattering. *Adv. Funct. Mater.* **22**, 1385–1390 (2012).
41. Liu, W., Sarkar, D., Kang, J., Cao, W. & Banerjee, K. Impact of contact on the operation and performance of back-gated monolayer MoS_2 field-effect-transistors. *ACS Nano* **9**, 7904–7912 (2015).
42. Smithe, K. K. H., English, C. D., Suryavanshi, S. V. & Pop, E. High-field transport and velocity saturation in synthetic monolayer MoS_2. *Nano Lett.* **18**, 4516–4522 (2018).
43. Smithe, K. K. H., Suryavanshi, S. V., Muñoz Rojo, M., Tedjarati, A. D. & Pop, E. Low variability in synthetic monolayer MoS_2 devices. *ACS Nano* **11**, 8456–8463 (2017).
44. Gurvitch, M. Ioffe-Regel criterion and resistivity of metals. *Phys. Rev. B* **24**, 7404–7407 (1981).
45. Chuang, H.-J. et al. Low-resistance 2D/2D ohmic contacts: a universal approach to high-performance WSe_2, MoS_2, and $MoSe_2$ transistors. *Nano Lett.* **16**, 1896–1902 (2016).
46. Ho, P.-H. et al. High-mobility InSe transistors: the role of surface oxides. *ACS Nano* **11**, 7362–7370 (2017).
47. Yu, Z. et al. Towards intrinsic charge transport in monolayer molybdenum disulfide by defect and interface engineering. *Nat. Commun.* **5**, 5290 (2014).
48. Chuang, H.-J. et al. High mobility WSe_2 p-and n-type field-effect transistors contacted by highly doped graphene for low-resistance contacts. *Nano Lett.* **14**, 3594–3601 (2014).
49. Dumcenco, D. et al. Large-area epitaxial monolayer MoS_2. *ACS Nano* **9**, 4611–4620 (2015).
50. Chen, J. et al. Chemical vapor deposition of high-quality large-sized MoS_2 crystals on silicon dioxide substrates. *Adv. Sci.* **3**, 1500033 (2016).

51. Song, J.-G. et al. Catalytic chemical vapor deposition of large-area uniform two-dimensional molybdenum disulfide using sodium chloride. *Nanotechnology* **28**, 465103 (2017).
52. Yang, P. et al. Batch production of 6-inch uniform monolayer molybdenum disulfide catalyzed by sodium in glass. *Nat. Commun.* **9**, 1–10 (2018).

Acknowledgements

We thank the Ministry of Science and Technology (MOST) Taiwan Grants MOST 107-2119-M-007-011-MY2 and MOST 106-2628-M-007-003-MY3, as well as the Academic Summit Project 107-2745-M-002-001-ASP. Financial supports by the i-MATE program in Academia Sinica, and the Center of Atomic Initiative for New Materials (AI-Mat), National Taiwan University (107L9008), from the Featured Areas Research Center Program within the framework of the Higher Education Sprout Project by the Ministry of Education (MOE) in Taiwan, are also acknowledged. The authors thank the TEM technical research services of NTU consortia of Key Technologies.

Author contributions

M.-C.C., P.-H.H., M.-F.T., and F.-Y.L. contributed equally to this work. P.-H.H., M.-C.C., and M.-F.T. designed the method. M.-C.C., M.-F.T., F.-Y.L., H.W., P.-P.H., C.-H.C., Y.-C.Y., and H.-Y.D. helped with the CVD process and optical spectroscopy. P.-H.H. fabricated the FET devices and took the electrical measurement. C.-H.H. and J.-J.S. helped with the XPS measurement. I.-K.L., I.-T.W., and C.-Y.W. helped the TEM measurement. P.-H.H. and M.-C.C. wrote the article and discussed with C.-W.C., L.-C.C., K.-H.C., and P.-W.C.

Competing interests

The authors declare no competing interests.

Additional information

Supplementary information is available for this paper at https://doi.org/10.1038/s41467-020-17517-6.

Correspondence and requests for materials should be addressed to P.-H.H., K.-H.C., P.-W.C. or L.-C.C.

Peer review information *Nature Communications* thanks Shisheng Li, Ynqing Wang, and Peng Yu for their contribution to the peer review of this work. Peer review reports are available.

Reprints and permission information is available at http://www.nature.com/reprints

Publisher's note Springer Nature remains neutral with regard to jurisdictional claims in published maps and institutional affiliations.

Open Access This article is licensed under a Creative Commons Attribution 4.0 International License, which permits use, sharing, adaptation, distribution and reproduction in any medium or format, as long as you give appropriate credit to the original author(s) and the source, provide a link to the Creative Commons license, and indicate if changes were made. The images or other third party material in this article are included in the article's Creative Commons license, unless indicated otherwise in a credit line to the material. If material is not included in the article's Creative Commons license and your intended use is not permitted by statutory regulation or exceeds the permitted use, you will need to obtain permission directly from the copyright holder. To view a copy of this license, visit http://creativecommons.org/licenses/by/4.0/.

© The Author(s) 2020